

Mass functions and bias of dark matter halos

P. Valageas

Institut de Physique Théorique, CEA Saclay, 91191 Gif-sur-Yvette, France

Received / Accepted

ABSTRACT

Aims. We revisit the study of the mass functions and the bias of dark matter halos.

Methods. Focusing on the limit of rare massive halos, we point out that exact analytical results can be obtained for the large-mass tail of the halo mass function. This is most easily seen from a steepest-descent approach, that becomes asymptotically exact for rare events. We also revisit the traditional derivation of the bias of massive halos, associated with overdense regions in the primordial density field.

Results. We check that the theoretical large-mass cutoff agrees with the mass functions measured in numerical simulations. For halos defined by a nonlinear threshold $\delta = 200$ this corresponds to using a linear threshold $\delta_L \simeq 1.59$ instead of the traditional value $\simeq 1.686$. We also provide a fitting formula that matches simulations over all mass scales and obeys the exact large-mass tail. Next, paying attention to the Lagrangian-Eulerian mapping (i.e. corrections associated with the motions of halos), we improve the standard analytical formula for the bias of massive halos. We check that our prediction, which contains no free parameter, agrees reasonably well with numerical simulations. In particular, it recovers the steepening of the dependence on scale of the bias that is observed at higher redshifts, which published fitting formulae did not capture. This behavior mostly arises from nonlinear biasing.

Key words. Cosmology: large-scale structure of Universe; gravitation; Methods: analytical

1. Introduction

The distribution of nonlinear virialized objects, such as galaxies or clusters of galaxies, is a fundamental test of cosmological models. First, this allows us to check the validity of the standard cosmological scenario for the formation of large-scale structures, where nonlinear objects form thanks to the amplification by gravitational instability of small primordial density fluctuations, built for instance by an early inflationary stage (e.g., Peebles 1993; Peacock 1998). For cold dark matter (CDM) scenarios (Peebles 1982), where the amplitude of the initial perturbations grows at smaller scales, this gives rise to a hierarchical process, where increasingly large and massive objects form as time goes on, as increasingly large scales turn nonlinear. This process has been largely confirmed by observations, which find smaller galaxies at very high redshifts (e.g., Trujillo et al. 2007) while massive clusters of galaxies (which are the largest bound objects in the Universe) appear at low redshifts (e.g., Borgani et al. 2001). Second, on a more quantitative level, statistical properties, such as the mass function and the two-point correlation of these objects, provide strong constraints on the cosmological parameters (e.g. through the linear growth factor $D_+(t)$ of density perturbations) and on the primordial fluctuations (e.g. through the initial density power spectrum $P_L(k)$). For these purposes, the most reliable constraints come from observations of the most massive objects (rare-event tails) at the largest scales. Indeed, in this regime the formation of large-scale structures is dominated by the gravitational dynamics (baryonic physics, which involves intricate processes associated with pressure effects, cooling and heating, mostly occurs at galactic scales and below), which further simplifies as one probes quasi-linear scales or rare events where effects asso-

ciated with multiple mergings can be neglected. Moreover, in this regime astrophysical objects, such as galaxies or clusters of galaxies, can be directly related to dark matter halos, and their abundance is highly sensitive to cosmological parameters thanks to the steep decline of the high-mass tail of the mass function (e.g., Evrard 1989).

Thus, the computation of the halo mass function (and especially its large-mass tail) has been the focus of many works, as it is one of the main properties measured in galaxy and cluster surveys that can be compared with theoretical predictions. Most analytical derivations follow the Press-Schechter approach (Press & Schechter 1974) or its main extension, the excursion set theory of Bond et al. (1991). In this framework, one attempts to estimate the number of virialized objects of mass M from the probability to have a linear density contrast δ_L at scale M above some given threshold δ_c . Thus, one identifies current nonlinear halos from positive density fluctuations in the initial (linear) density field, on a one-to-one basis. This is rather well justified for rare massive objects, where one can expect such a link to be valid since such halos should have remained well-defined objects until now (as they should have suffered only minor mergers). By contrast, small and typical objects have experienced many mergers and should be sensitive to highly non-local effects (e.g. tidal forces, mergers), so that such a direct link should no longer hold, as can be checked in numerical simulations (Bond et al. 1991). As noticed by Press & Schechter (1974), the simplest procedure only yields half the mass of the Universe in such objects (essentially because only half of the Gaussian initial fluctuations have a positive density contrast, whatever the smoothing scale), which they corrected by an ad-hoc multiplicative factor 2. In this respect the main result of the excursion set theory

was to provide an analytical derivation of this missing factor 2, in the simplified case of a top-hat filter in Fourier space (Bond et al. 1991). Then, it arises from the fact that objects of mass larger than M are associated with configurations such that the linear density contrast goes above the threshold δ_c at some scale $M' \geq M$, which includes cases missed by the Press-Schechter prescription where the linear density contrast decreases below this scale M' so that $\delta_L < \delta_c$ at scale M (“cloud-in-cloud” problem). The characteristic threshold δ_c is usually taken as the linear density contrast reached when the spherical collapse dynamics predicts collapse to a zero radius. In an Einstein-de Sitter universe this corresponds to $\delta_c \simeq 1.686$ and to a nonlinear density contrast $\delta \simeq 177$ (assuming full virialization in half the turn-around radius). This linear threshold only shows a very weak dependence on cosmological parameters.

Numerical simulations have shown that the Press-Schechter mass function (PS) is reasonably accurate, especially in view of its simplicity. Thus, it correctly predicts the typical mass scale of virialized halos at any redshift, as could be expected since the large-mass behavior is rather well justified. In addition, it predicts a universal scaling that appears to be satisfied by the mass functions measured in simulations, that is, the dependence on halo mass, redshift and cosmology is fully contained in the ratio $\nu = \delta_c/\sigma(M, z)$, where $\sigma(M, z)$ is the rms linear density fluctuation at scale M . However, as compared with numerical results it overestimates the low-mass tail and it underestimates the high-mass tail. This has led to many numerical studies which have provided various fitting formulae for the mass function of virialized halos, written in terms of the scaling variable ν (or σ) (Sheth & Tormen 1999; Jenkins et al. 2001; Reed et al. 2003; Warren et al. 2006; Tinker et al. 2008). We may note here that a theoretical approach that attempted to improve over the PS mass function was to consider the ellipsoidal collapse dynamics, to take into account the deviations from spherical symmetry for intermediate mass halos (Sheth et al. 2001). However, as described in the original paper (and emphasized in Robertson et al. 2009), at large mass one recovers the spherical collapse so that this cannot cure the underestimate in the far tail. Therefore, one often builds fitting formulae from numerical simulations, while keeping the form of the large-mass exponential cutoff, but treating δ_c as a free parameter.

A second property of virialized halos that can be used to constrain cosmological models, beyond their number density, is their two-point correlation. Indeed, observations show that galaxies and clusters do not obey a Poisson distribution but show significant large-scale correlations (e.g., McCracken et al. 2008; Padilla et al. 2004). In particular, their two-point correlation roughly follows the underlying matter correlation, up to a multiplicative factor b^2 , called the bias, that grows for more massive and extreme objects. Following the spirit of the Press-Schechter picture, Kaiser (1984) found that this behavior arises in a natural fashion if halos are associated with large overdensities in the Gaussian initial (linear) density field, above the threshold δ_c . This was further expanded by Bardeen et al. (1986) and Bond & Myers (1996), who considered the clustering of peaks in the Gaussian linear density field. A simpler derivation, based on a peak-background split argument, and taking care of the mapping from Lagrangian to Eulerian space, was presented in Mo & White (1996). It provides a prediction for the bias

$b(M)$ as a function of halo mass, in the limit of large distance, $r \rightarrow \infty$, that agrees reasonably well with numerical simulations. However, as for the PS mass function, in order to improve the agreement with numerical results various fitting formulae have been proposed (Sheth & Tormen 1999; Hamana et al. 2001; Pillepich et al. 2009). Again, since the ellipsoidal collapse model reduces to the spherical dynamics for rare massive halos, it also requires free parameters to improve its accuracy, but the latter are consistent with those used for the mass function (Sheth et al. 2001).

In this article we revisit the derivation of the mass function and the bias of rare massive halos, following the spirit of the Press & Schechter (1974) and Kaiser (1984) approaches. That is, we use the fact that large halos can be identified from overdensities in the Gaussian initial (linear) density field. First, we briefly review in section 2 some properties of the growth of linear fluctuations and of the spherical dynamics in Λ CDM cosmologies. Next, we recall in section 3 that in the quasi-linear regime (i.e. at large scales), the probability distribution of the nonlinear density contrast δ_r within spherical cells of radius r can be obtained from spherical saddle-points of a specific action \mathcal{S} , for moderate values of δ_r where shell-crossing does not come into play. We also discuss the properties of these saddle-points as a function of mass, scale and redshift. Then, we point out in section 4 that this provides the exact exponential tail of the halo mass function. This applies to any nonlinear density contrast threshold δ that is used to define halos, provided it is below the upper bound δ_+ where shell-crossing comes into play. We compare our results with numerical simulations and we give a fitting formula that applies over all mass scales and satisfies the exact large-mass cutoff. Next, we recall in section 5 that these results also provide the density profile of dark matter halos at outer radii (i.e. beyond the virial radius) in the limit of large mass. Finally, we study the bias of massive halos in section 6, paying attention to some details such as the Lagrangian-Eulerian mapping, and we compare our results with numerical simulations. We conclude in section 7.

2. Linear perturbations and spherical dynamics

We consider in this article a flat CDM cosmology with two components, (i) a non-relativistic component (dark and baryonic matter, which we do not distinguish here) that clusters through gravitational instability, and (ii) an uniform dark energy component that does not cluster at the scales of interest, with an equation-of-state parameter $w = p_{\text{de}}/\rho_{\text{de}}$. For the numerical computations we shall focus on a Λ CDM cosmology, where the dark energy is associated with a cosmological constant that is exactly uniform with $w = -1$. However, our results directly extend to curved universes (i.e. $\Omega_k \neq 0$) and to dark energy models with a possibly time-varying $w(z)$, as long as we can neglect the dark energy fluctuations on the scales of interest, which is valid for realistic cases. Focussing on the case of constant w , we first recall in this section the equations that describe the dynamics of the background and of linear matter density perturbations, as well as the nonlinear spherical dynamics.

The evolution of the scale factor $a(t)$ is determined by the Friedmann equation (Wang & Steinhardt 1998),

$$\frac{H^2(t)}{H_0^2} = \Omega_{\text{m}0} a^{-3} + \Omega_{\text{de}0} a^{-3-3w}, \quad \text{with } H(t) = \frac{\dot{a}}{a}, \quad (1)$$

where subscripts 0 denote current values at $z = 0$, when $a = 1$, and a dot denotes the derivative with respect to cosmic time t . On the other hand, the density parameters vary with time as

$$\Omega_m(a) = \frac{\Omega_{m0}}{\Omega_{m0} + \Omega_{de0} a^{-3w}}, \quad \Omega_{de}(a) = \frac{\Omega_{de0}}{\Omega_{m0} a^{3w} + \Omega_{de0}}. \quad (2)$$

Next, introducing the matter density contrast, $\delta(\mathbf{x}, t) = (\rho_m(\mathbf{x}, t) - \bar{\rho}_m) / \bar{\rho}_m$, where $\bar{\rho}_m(t)$ is the mean matter density, linear density fluctuations grow as

$$\ddot{\delta}_L + 2\frac{\dot{a}}{a}\dot{\delta}_L - 4\pi\mathcal{G}\bar{\rho}_m\delta_L = 0, \quad (3)$$

where the subscript L denotes linear quantities. For numerical purposes it is convenient to use the logarithm of the scale factor as the time variable. Then, using the Friedmann equation (1) the linear growth factor $D_+(t)$ evolves from Eq.(3) as

$$D_+'' + \left[\frac{1}{2} - \frac{3}{2}w\Omega_{de}\right] D_+' - \frac{3}{2}\Omega_m D_+ = 0, \quad (4)$$

where we note with a prime the derivative with respect to $\ln a$, as $D_+' = dD_+/d\ln a$. Then, the normalized linear growth factor, $g(t)$, defined as

$$g(t) = \frac{D_+(t)}{a(t)} \quad \text{and} \quad g(t=0) = 1, \quad (5)$$

obeys

$$g'' + \left[\frac{5}{2} - \frac{3}{2}w\Omega_{de}\right] g' + \frac{3}{2}(1-w)\Omega_{de}g = 0, \quad (6)$$

with the initial conditions $g \rightarrow 1$ and $g' \rightarrow 0$ at $a \rightarrow 0$.

In the following we shall also need the dynamics of spherical density fluctuations. For such spherically symmetric initial conditions, the physical radius $r(t)$, that contains the constant mass M until shell-crossing, evolves as

$$\ddot{r} = -\frac{4\pi\mathcal{G}}{3}r[\rho_m + (1+3w)\bar{\rho}_{de}] \quad \text{with} \quad \rho_m = \frac{3M}{4\pi r^3}. \quad (7)$$

Note that ρ_m is the mean density within the sphere of radius r (and not the local density at radius r). Using again the Friedmann equation (1) this reads as

$$r'' - \frac{3}{2}(1+w\Omega_{de})r' + \frac{\rho_m + (1+3w)\bar{\rho}_{de}}{2(\bar{\rho}_m + \bar{\rho}_{de})}r = 0. \quad (8)$$

As for the linear growth factor $D_+(t)$, it is convenient to introduce the normalized radius $y(t)$ defined as

$$y(t) = \frac{r(t)}{q(t)} \quad \text{and} \quad q(t) \propto a(t), \quad y(t=0) = 1. \quad (9)$$

Thus, $q(t)$ is the Lagrangian coordinate of the shell $r(t)$, that is, the physical radius that would enclose the same mass M in a uniform universe with the same cosmology. This also implies that the density ρ_m writes as

$$\rho_m(t) = \bar{\rho}_m(t)y(t)^{-3}. \quad (10)$$

Then, Equation (8) leads to

$$y'' + \left[\frac{1}{2} - \frac{3}{2}w\Omega_{de}\right]y' + \frac{\Omega_m}{2}(y^{-3} - 1)y = 0. \quad (11)$$

Of course, we can check that in the linear regime, where $y_L = 1 - \delta_L/3$, we recover Eq.(4) for the linear growth of δ_L . Then, to obtain the nonlinear density contrast, $\delta(z) = \rho_m/\bar{\rho}_m - 1$, associated with the linear density contrast, $\delta_L(z)$, at a given redshift z , we solve Eq.(11) with the initial condition $y(z_i) = 1 - \delta_{Li}/3$ and $y'(z_i) = -\delta_{Li}/3$ at some high redshift z_i , with $\delta_{Li}/\delta_L = D_+(z_i)/D_+(z)$. For any redshift z this defines a mapping $\delta_L \mapsto \delta = \mathcal{F}(\delta_L)$ that fully describes the spherical dynamics before shell-crossing.

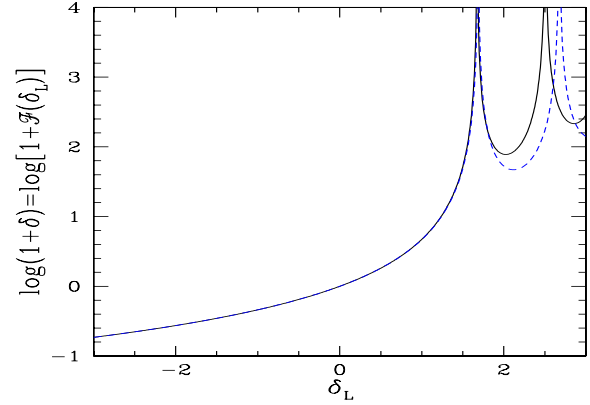


Fig. 1. The function $\mathcal{F}(\delta_L)$ that describes the spherical dynamics when there is no shell-crossing, at $z = 0$. The solid line corresponds to the Λ CDM cosmology (with $\Omega_{m0} = 0.27$) and the dashed line to the Einstein-de Sitter case $\Omega_{m0} = 1$. The second peak corresponds to a second collapse to the center, but for our purposes we only need $\mathcal{F}(\delta_L)$ before first collapse.

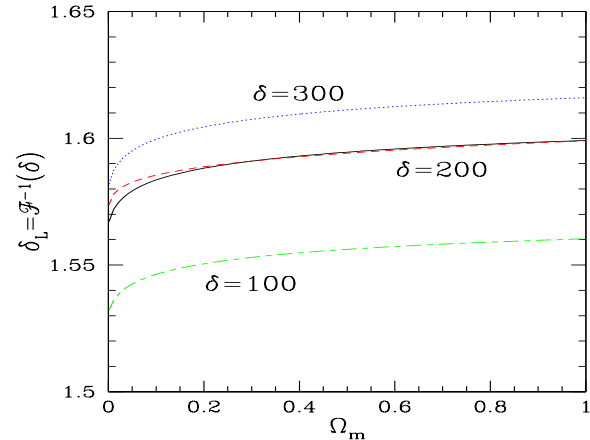


Fig. 2. The linear density contrast $\delta_L = \mathcal{F}^{-1}(\delta)$ associated with the nonlinear density contrast δ , through the spherical dynamics, as a function of the cosmological parameter $\Omega_m(z)$ at the redshift of interest. We show the three cases $\delta = 100, 200$ and 300 . The dashed line is the fit (12) to the case $\delta = 200$.

We compare in Fig. 1 the function $\mathcal{F}(\delta_L)$ obtained at $z = 0$ within the Λ CDM cosmology that we consider in this article (solid line) with the Einstein-de Sitter case (dashed

line), where it has a well-known parametric form (Peebles 1980). As is well known, we can check that the dependence on Ω_{m0} is very weak until full collapse to a point, which occurs at slightly lower values of δ_L for low Ω_{m0} . We show in Fig. 2 the linear density contrasts, $\delta_L = \mathcal{F}^{-1}(\delta)$, associated with three nonlinear density contrasts, $\delta = 100, 200$ and 300 , as a function of the cosmological parameter $\Omega_m(z)$. In agreement with Fig. 1, they show a slight decrease for smaller Ω_m . For $\delta = 200$ a simple fit (dashed line) is provided by

$$\delta = 200 : \quad \delta_L \simeq 1.567 + 0.032 (\Omega_m + 0.0005)^{0.24}, \quad (12)$$

which agrees with the exact curve to better than 5×10^{-4} for $\Omega_m > 0.2$, which covers the range of practical interest.

In this article we consider Gaussian initial fluctuations, which are fully defined by the linear density power spectrum

$$\langle \tilde{\delta}_L(\mathbf{k}_1) \tilde{\delta}_L(\mathbf{k}_2) \rangle = \delta_D(\mathbf{k}_1 + \mathbf{k}_2) P_L(k_1), \quad (13)$$

where δ_D is the Dirac distribution and we normalized the Fourier transform as

$$\delta(\mathbf{x}) = \int d\mathbf{k} e^{i\mathbf{k}\cdot\mathbf{x}} \tilde{\delta}(\mathbf{k}), \quad (14)$$

where \mathbf{x} and \mathbf{k} are the comoving spatial coordinate and wavenumber. This gives for the linear density two-point correlation

$$\begin{aligned} C_L(\mathbf{x}_1, \mathbf{x}_2) &= \langle \delta_L(\mathbf{x}_1) \delta_L(\mathbf{x}_2) \rangle \\ &= 4\pi \int dk k^2 P_L(k) \frac{\sin(k|\mathbf{x}_2 - \mathbf{x}_1|)}{k|\mathbf{x}_2 - \mathbf{x}_1|}. \end{aligned} \quad (15)$$

We also introduce the smoothed density contrast, $\delta_r(\mathbf{x})$, within the sphere of radius r and volume V around position \mathbf{x} ,

$$\delta_r(\mathbf{x}) = \int_V \frac{d\mathbf{x}'}{V} \delta(\mathbf{x} + \mathbf{x}') = \int d\mathbf{k} e^{i\mathbf{k}\cdot\mathbf{x}} \tilde{\delta}(\mathbf{k}) \tilde{W}(kr), \quad (16)$$

with a top-hat window that reads in Fourier space as

$$\tilde{W}(kr) = \int_V \frac{d\mathbf{x}}{V} e^{i\mathbf{k}\cdot\mathbf{x}} = 3 \frac{\sin(kr) - kr \cos(kr)}{(kr)^3}. \quad (17)$$

Then, in the linear regime, the cross-correlation of the smoothed linear density contrast at scales r_1 and r_2 and positions \mathbf{x}_1 and $\mathbf{x}_2 = \mathbf{x}_1 + \mathbf{x}$ reads as

$$\begin{aligned} \sigma_{r_1, r_2}^2(x) &= \langle \delta_{Lr_1}(\mathbf{x}_1) \delta_{Lr_2}(\mathbf{x}_1 + \mathbf{x}) \rangle \\ &= 4\pi \int dk k^2 P_L(k) \tilde{W}(kr_1) \tilde{W}(kr_2) \frac{\sin(kx)}{kx}. \end{aligned} \quad (18)$$

In particular, $\sigma_r = \sigma_{r,r}(0)$ is the usual rms linear density contrast at scale r .

3. Distribution of the density contrast

We recall here that in the quasi-linear limit, $\sigma_r \rightarrow 0$, the distribution $\mathcal{P}(\delta_r)$ of the nonlinear density contrast δ_r at scale r can be derived from a steepest-descent method (Valageas 2002a). In agreement with the alternative approach of Bernardeau (1994a), this shows that rare-event tails are dominated by spherical saddle-points, which we use in sections 4-6 to obtain the properties of massive halos.

Since the system is statistically homogeneous we can consider the sphere of radius r centered on the origin $\mathbf{x} = 0$. Then, we first introduce the cumulant generating function $\varphi(y)$,

$$e^{-\varphi(y)/\sigma_r^2} = \langle e^{-y\delta_r/\sigma_r^2} \rangle = \int_{-1}^{\infty} d\delta_r e^{-y\delta_r/\sigma_r^2} \mathcal{P}(\delta_r), \quad (19)$$

which determines the distribution $\mathcal{P}(\delta_r)$ through the inverse Laplace transform

$$\mathcal{P}(\delta_r) = \int_{-i\infty}^{+i\infty} \frac{dy}{2\pi i \sigma_r^2} e^{[y\delta_r - \varphi(y)]/\sigma_r^2}. \quad (20)$$

In Eq.(19) we rescaled the cumulant generating function by a factor σ_r^2 so that it has a finite limit in the quasi-linear limit $\sigma_r \rightarrow 0$ for the Gaussian initial density fluctuations that we study in this article (Bernardeau et al. 2002). In particular, its expansion at $y = 0$ reads as

$$\varphi(y) = - \sum_{p=2}^{\infty} \frac{(-y)^p}{p!} \frac{\langle \delta_r^p \rangle_c}{\sigma_r^{2(p-1)}}. \quad (21)$$

Then, the average (19) can be written as the path integral

$$e^{-\varphi(y)/\sigma_r^2} = (\det C_L^{-1})^{1/2} \int \mathcal{D}\delta_L(\mathbf{q}) e^{-\mathcal{S}[\delta_L]/\sigma_r^2}, \quad (22)$$

where C_L^{-1} is the inverse matrix of the two-point correlation (15) and the action \mathcal{S} reads as

$$\mathcal{S}[\delta_L] = y \delta_r[\delta_L] + \frac{\sigma_r^2}{2} \delta_L \cdot C_L^{-1} \cdot \delta_L \quad (23)$$

Here $\delta_r[\delta_L]$ is the nonlinear functional that affects to the initial condition defined by the linear density field $\delta_L(\mathbf{q})$ the nonlinear density contrast δ_r within the sphere of radius r , and we note $\delta_L \cdot C_L^{-1} \cdot \delta_L = \int d\mathbf{q}_1 d\mathbf{q}_2 \delta_L(\mathbf{q}_1) C_L^{-1}(\mathbf{q}_1, \mathbf{q}_2) \delta_L(\mathbf{q}_2)$. Note that the action \mathcal{S} does not depend on the normalization of the linear power spectrum since both σ_r^2 and C_L are proportional to P_L .

In the quasi-linear limit, $\sigma_r \rightarrow 0$, as shown in Valageas (2002a) the path integral (22) is dominated by the minimum¹ of the action $\mathcal{S}[\delta_L]$,

$$\sigma_r \rightarrow 0 : \quad \varphi(y) \rightarrow \min_{\delta_L(\mathbf{q})} \mathcal{S}[\delta_L]. \quad (24)$$

Using the spherical symmetry of the top-hat window W , in agreement with the approach of Bernardeau (1994a), one obtains a spherical saddle-point with the radial profile

$$\delta_{Lq'} = \delta_{Lq} \frac{\sigma_{q,q'}}{\sigma_q^2}, \quad (25)$$

where $\sigma_{q,q'} = \sigma_{q,q'}(0,0)$ and q is the Lagrangian coordinate associated with the Eulerian radius r through the spherical dynamics recalled in section 2, and q' is a dummy Lagrangian coordinate along the radial profile (hereafter we denote by the letter q Lagrangian radii, which are associated with the linear density field, whereas r denotes

¹ As described in details in Valageas (2002a), depending on the slope of the linear power spectrum the saddle-point (25) may only be a local minimum or maximum, but it still governs the rare-event limit, in agreement with physical expectations.

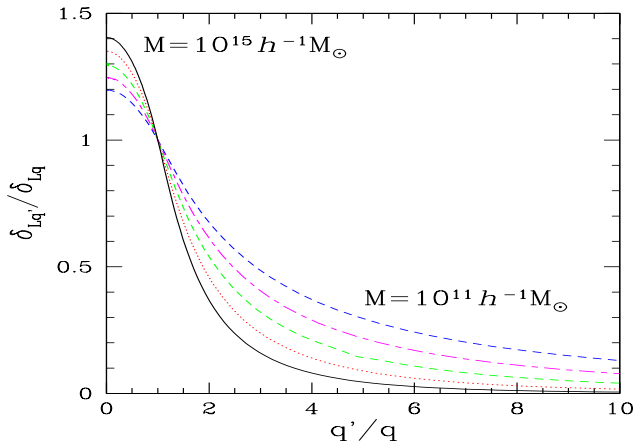


Fig. 3. The radial profile (25) of the linear density contrast $\delta_{Lq'}$ of the saddle point of the action $\mathcal{S}[\delta_L(\mathbf{q})]$. We show the profiles obtained with a Λ CDM cosmology for the masses $M = 10^{11}, 10^{12}, 10^{13}, 10^{14}$ and $10^{15} h^{-1} M_{\odot}$. A larger mass corresponds to a lower ratio $\delta_{Lq'}/\delta_{Lq}$ at large radii $q'/q > 1$.

Eulerian radii associated with the nonlinear density contrast δ_r). Thus, the radii q' and r' are related by

$$q'^3 = (1 + \delta_{r'}) r'^3, \quad \text{with} \quad \delta_{r'} = \mathcal{F}(\delta_{Lq'}), \quad (26)$$

where the function $\delta_{r'} = \mathcal{F}(\delta_{Lq'})$, that describes the spherical dynamics, was obtained below Eq.(11) and shown in Fig. 1.

We can note that the profile (25) is also the mean conditional profile of the linear density contrast $\delta_{Lq'}$, under the constraint that it is equal to a given value δ_{Lq} at a given radius q (e.g., Bernardeau 1994a). The reason why the nonlinear dynamics gives back this result is that the nonlinear density contrast δ_r only depends on the linear density contrast δ_{Lq} at the associated Lagrangian radius q , through the mapping $\delta_r = \mathcal{F}(\delta_{Lq})$. Indeed, as long as shell-crossing does not modify the mass enclosed within the shell of Lagrangian coordinate q , its dynamics is independent of the motion of inner and outer shells (thanks to Gauss theorem). Then, in order to obtain the minimum of the action \mathcal{S} we could proceed in two steps. First, for arbitrary Lagrangian radius q and linear contrast δ_{Lq} , we minimize \mathcal{S} with respect to the profile $\delta_{Lq'}$ over $q' \neq q$. From the previous argument, only the second Gaussian term in (23) varies so that this partial minimization leads to the profile (25) (indeed, for Gaussian integrals the saddle-point method is exact). Second, we minimize over the Lagrangian radius q (or equivalently over δ_L or δ_r), which leads to Eq.(29) below. Here we also use the fact that a spherical saddle-point with respect to spherical fluctuations is automatically a saddle-point with respect to arbitrary non-spherical perturbations and it can be seen that for small y one obtains a minimum (then we assume that at finite y strong deviations from spherical symmetry do not give rise to deeper minima, which seems natural from physical expectations). We refer to Valageas (2002a,2009b) for more detailed derivations.

Note that the shape of the linear profile (25) depends on the shape of the linear power spectrum, whence on the mass scale M of the saddle point for a curved CDM linear power spectrum, but not on redshift. We show in Fig. 3 the profile (25) obtained for several masses M . For a power-law

linear power spectrum, of slope n , Eq.(25) leads to $\delta_{Lq'} \propto q'^{-(n+3)}$ at large radii, $q' \rightarrow \infty$. Then, since for a CDM cosmology n increases at larger scales, the profile shows a steeper falloff at large radii for larger mass, in agreement with Fig. 3 (in this section we consider a Λ CDM cosmology with $(\Omega_{m0}, \Omega_{\Lambda0}, \sigma_8, n_s, h) = (0.27, 0.73, 0.79, 0.95, 0.7)$).

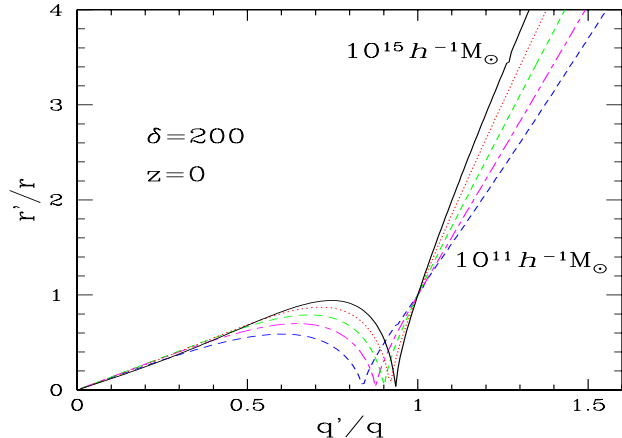


Fig. 4. The Lagrangian map $q' \mapsto r'$ given by the spherical dynamics (neglecting shell-crossing) for the saddle-point (25) with a nonlinear density contrast $\delta = 200$ at the Eulerian radius r . We plot the curves obtained at $z = 0$ for several masses, as in Fig. 3. Inner shells have already gone once through the center (hence their dynamics is no longer exactly given by Eq.(11)) but they have not crossed the radius r yet.

We show in Fig. 4 the Lagrangian map, $q' \mapsto r'$, given by the spherical dynamics (i.e. the function $\mathcal{F}(\delta_L)$ where we neglect shell-crossing) for the saddle-point (25), with a nonlinear density contrast $\delta = 200$ at the Eulerian radius r , at redshift $z = 0$. Inner shells have already gone once through the center but they have not reached radius r yet. Even though their dynamics is no longer exactly given by Eq.(11), an exact computation would give the same property as the increasing mass seen by these particles, as they pass outer shells, should slow them down as compared with the constant-mass dynamics. In agreement with Fig. 3, for larger masses, which have a larger central linear density contrast, shell-crossing has moved to larger radii (the local maximum of r'/r , to the left of $r' = 0$, is higher).

From the Lagrangian map, $q' \mapsto r'$, we define the nonlinear density threshold, δ_+ , as the nonlinear density contrast δ_r reached within radius r at the time when inner shells first cross this radius r . Then, up to δ_+ , the mass within the Lagrangian shell q has remained constant, so that the saddle-point (25)-(26) is exact (this slightly underestimates δ_+ as the expansion of inner shells should be somewhat slowed down by the mass of the outer shells they have overtaken). We show in Fig. 5 the dependence on redshift of this threshold δ_+ , for several masses. In agreement with Figs. 3, 4, this threshold is smaller for larger masses. It shows a slight decrease at higher redshift as $\Omega_m(z)$ grows to unity. We can see that for massive clusters at $z = 0$, which have a mass of order $10^{15} h^{-1} M_{\odot}$, the density contrast $\delta \simeq 200$ should separate outer shells with radial accretion from inner shells with a significant transverse velocity dispersion, built

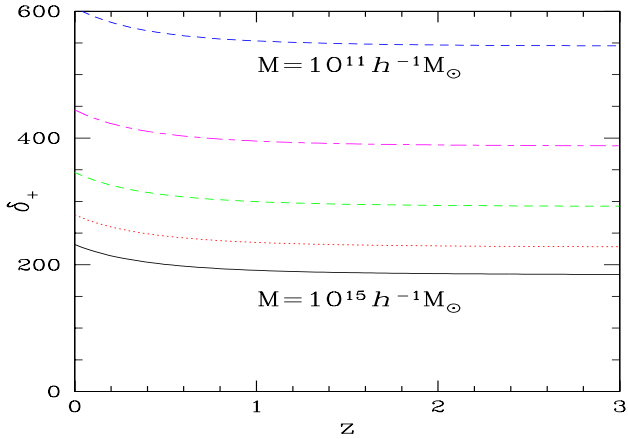


Fig. 5. The nonlinear density contrast δ_+ , beyond which shell-crossing must be taken into account, as a function of redshift for several mass scales.

by the radial-orbit instability that dominates the dynamics after shell-crossing, see Valageas 2002b (in particular the appendix A). This agrees with numerical simulations, see for instance the lower panel of Fig.3 in Cuesta et al. (2008), which show that rare massive clusters exhibit a strong radial infall pattern, with a low velocity dispersion, beyond the virial radius (where $\delta_r \sim 200$), while inner radii show a large velocity dispersion (even though we can distinguish close to the virial radius the outward velocity associated with the shells that have gone once through the center). Small-mass halos do not show such a clear infall pattern and the velocity dispersion is significant at all radii (e.g., upper panel of Fig.3 in Cuesta et al. 2008). This expresses the fact that such halos, associated with typical events and moderate density fluctuations, are no longer governed by the spherical saddle-point (25). Indeed, at low mass and small Lagrangian radius q , σ_q is no longer very small so that the path integral (22) is no longer dominated by its minimum and one must integrate over all typical initial conditions, including large deviations from spherical symmetry.

Next, the amplitude δ_{Lq} and the minimum φ are given as functions of y by the implicit equations (Legendre transform)

$$y = -\tau \frac{d\tau}{d\mathcal{G}} \quad \text{and} \quad \varphi = y\mathcal{G} + \frac{\tau^2}{2}, \quad (27)$$

where the function $\tau(\mathcal{G})$ is defined from the spherical dynamics through the parametric system (Valageas 2002a; Bernardeau 1994b)

$$\mathcal{G} = \delta_r = \mathcal{F}(\delta_{Lq}) \quad \text{and} \quad \tau = -\delta_{Lq} \frac{\sigma_r}{\sigma_q}. \quad (28)$$

The system (27) also reads as

$$\varphi = \min_{\mathcal{G}} \left[y\mathcal{G} + \frac{\tau^2(\mathcal{G})}{2} \right]. \quad (29)$$

Note that the function $\tau(\mathcal{G})$, whence the cumulant generating function $\varphi(y)$, depends on the shape of the linear power spectrum through the ratio of linear power σ_r/σ_q at Eulerian and Lagrangian scales r and q . Finally, from the

inverse Laplace transform (20), a second steepest-descent integration over the variable y gives (Valageas 2002a)

$$\sigma_r \rightarrow 0 : \quad \mathcal{P}(\delta_r) \sim e^{-\tau^2/(2\sigma_r^2)} = e^{-\delta_{Lq}^2/(2\sigma_q^2)}. \quad (30)$$

Thus, in the quasi-linear limit, the distribution $\mathcal{P}(\delta_r)$ is governed at leading order by the Gaussian weight of the linear fluctuation δ_{Lq} that is associated with the nonlinear density contrast δ_r through the spherical dynamics. We can note that Eq.(30) could also be obtained from a Lagrange multiplier method, without introducing the generating function $\varphi(y)$. Indeed, in the rare-event limit, where $\mathcal{P}(\delta)$ is governed by a single (or a few) initial configuration, we may write

$$\text{rare events : } \mathcal{P}(\delta) \sim \max_{\{\delta_L[\mathbf{q}] | \delta_r[\delta_L] = \delta\}} e^{-\frac{1}{2}\delta_L \cdot C_L^{-1} \cdot \delta_L}. \quad (31)$$

That is, $\mathcal{P}(\delta)$ is governed by the maximum of the Gaussian weight $e^{-(\delta_L \cdot C_L^{-1} \cdot \delta_L)/2}$ subject to the constraint $\delta_r[\delta_L] = \delta$ (assuming there are no degenerate maxima). Then, we can obtain this maximum by minimizing the action $\mathcal{S}[\delta_L]/\sigma_r^2$ of Eq.(23), where y plays the role of a Lagrange multiplier. This gives the saddle-point (25), and the amplitude δ_{Lq} and the radius q are directly obtained from the constraint $\delta = \mathcal{F}(\delta_{Lq})$, as in Eq.(26). Then, we do not need the explicit expression of the Lagrange multiplier y , as this is sufficient to obtain the last expression of the asymptotic tail (30). Nevertheless, it is useful to introduce the generating function $\varphi(y)$, which makes it clear that the Lagrange multiplier y is also the Laplace conjugate of the nonlinear density contrast δ as in Eq.(19), since it is also of interest by itself, as it yields the density cumulants through the expansion (21).

The asymptotic (30) holds in the rare-event limit. This corresponds to both the quasi-linear limit, $\sigma_r \rightarrow 0$ at fixed density contrast δ_r , and to the low-density limit, $\delta_r \rightarrow 0$ at fixed σ_r , as long as there is no shell-crossing. This latter requirement gives a lower boundary δ_- , for linear power spectra with a slope $n > -1$, and an upper boundary δ_+ , for any linear spectrum (Valageas 2002b). This upper boundary was shown in Fig. 5 for a Λ CDM cosmology, for several masses.

Indeed, at large positive density contrast, shell-crossing always occurs, as seen in Figs. 4-5. This invalidates the mapping $\delta_L \mapsto \delta = \mathcal{F}(\delta_L)$ obtained from Eq.(11), as mass is no longer conserved within the Lagrangian shell q , so that the asymptotic behavior (30) is no longer exact. In fact, as shown in Valageas (2002b), after shell-crossing it is no longer sufficient to follow the spherical dynamics, even if we take into account shell-crossing. Indeed, a strong radial-orbit instability develops so that the sensitivity to initial perturbations actually diverges when particles cross the center of the halo. Then, the functional $\delta_r[\delta_L(\mathbf{q})]$ is singular at such spherical states (i.e. it is discontinuous as infinitesimal deviations from spherical symmetry lead to a finite change of δ_r) and the path integral (22) is no longer governed by spherical states that have a zero measure. As noticed above, this also means that, in the limit of rare massive halos, the nonlinear density threshold δ_+ separates outer shells with a smooth radial flow from inner shells with a significant transverse velocity dispersion. Thus, δ_+ marks the virialization radius where isotropization of the velocity tensor becomes important, in agreement with numerical simulations (e.g., Cuesta et al. 2008).

It is interesting to note that a similar approach can be developed for the “adhesion model” (Gurbatov et al. 1989), where particles move according to the Zeldovich dynamics (Zeldovich 1970) but do not cross because of an infinitesimal viscosity (i.e. they follow the Burgers dynamics in the inviscid limit). Moreover, in the one-dimensional case, with a linear power-spectrum slope $n = -2$ or $n = 0$ (i.e. the linear velocity is a Brownian motion or a white noise), it is possible to derive the exact distribution $\mathcal{P}(\delta_r)$ by other techniques and to check that it agrees with the asymptotic tail (30), as seen in Valageas (2009a,b).

4. Mass function of collapsed halos

The quasi-linear limit (30) of the distribution $\mathcal{P}(\delta_r)$ clearly governs the large-mass tail of the mass function $n(M)dM$, where we define halos as spherical objects with a fixed density contrast $\delta_r = \delta$. Indeed, since the Lagrangian radius q is related to the halo mass by $M = \bar{\rho}_m 4\pi q^3/3$, massive halos correspond to large Eulerian and Lagrangian radii, and the limit $M \rightarrow \infty$ corresponds to the quasi-linear limit $\sigma_r \rightarrow 0$. Then, going from the distribution $\mathcal{P}(\delta_r)$ to the mass function $n(M)$ can introduce geometrical power-law prefactors since halos are not exactly centered on the cells of a fixed grid, as discussed in Betancort-Rijo & Montero-Dorta (2006), but the exponential cutoff remains the same as in Eq.(30), whence

$$M \rightarrow \infty : \ln[n(M)] \sim -\frac{\delta_L^2}{2\sigma^2}, \quad \text{with } \delta_L = \mathcal{F}^{-1}(\delta), \quad (32)$$

where $\sigma = \sigma_q$ with $M = \bar{\rho}_m 4\pi q^3/3$. A simple approximation for the mass function that satisfies this large-mass falloff can be obtained from the Press-Schechter method (PS), see Press & Schechter (1974), but using the actual linear threshold $\delta_L = \mathcal{F}^{-1}(\delta)$ associated with the nonlinear threshold δ that defines the halo radius r , rather than the linear threshold $\delta_c \simeq 1.686$ associated with the spherical collapse down to a point. This yields for the number of halos in the range $[M, M + dM]$ per unit volume,

$$n(M) dM = \frac{\bar{\rho}_m}{M} f(\sigma) \left| \frac{d\sigma}{\sigma} \right|, \quad (33)$$

with

$$f(\sigma) = \sqrt{\frac{2}{\pi}} \frac{\delta_L}{\sigma} e^{-\delta_L^2/(2\sigma^2)}. \quad (34)$$

The mass function (34) includes the usual prefactor 2 that gives the normalization

$$\int_0^\infty \frac{d\sigma}{\sigma} f(\sigma) = 1, \quad (35)$$

which ensures that all the mass is contained in such halos. However, we must note that the power-law prefactor in (34) has no strong theoretical justification since only the exponential cutoff (32) was exactly derived from (30). In principle, it could be possible to derive subleading terms (whence power-law prefactors) in the quasi-linear limit for $\mathcal{P}(\delta_r)$, by expanding the path integral (22) around the saddle-point (25). Then, one would also need to take more care of the prefactors that would arise as one goes from the distribution $\mathcal{P}(\delta_r)$ to the mass function $n(M)$. However, this expansion

would not allow one to derive the shape of the mass function at low masses, as this regime is far from the quasi-linear limit and involves multiple mergers far from spherical symmetry. Until a new method is devised to handle this regime, one must treat the prefactors as free parameters to be fitted to numerical simulations, in order to describe the mass function from small to large masses.

As for the probability distribution $\mathcal{P}(\delta_r)$, it is interesting to note that a similar high-mass tail can be derived for the “adhesion model”, where halos are defined as zero-size objects (shocks). Again, in the one-dimensional case, for $n = -2$ or $n = 0$ where the exact mass function can be obtained by other means, one can check that it agrees with the analog of the asymptotic tail (32) (Valageas 2009a,b,c).

We can note that the explanation of the large-mass tail (32) by the exact asymptotic result of the steepest-descent method described in section 3 agrees nicely with numerical simulations. This is most clearly seen in Figs. 3 and 6 of Robertson et al. (2009), who trace back the linear density contrast δ_L of the Lagrangian regions that form halos at $z = 0$. Their results show that the distribution of linear contrasts δ_L , measured as a function of mass (or of $\sigma(M)$), has a roughly constant lower bound δ_L^- , with $\delta_L^- \sim 1.59$ slightly lower than 1.686, and an upper bound δ_L^+ that grows with $\sigma(M)$. They obtain the same results when they define halos by nonlinear density contrasts $\delta = 100$ or $\delta = 600$, with a lower bound δ_L^- that grows somewhat with δ . In terms of the approach described above, this behavior expresses the fact that the most probable way to build a massive halo of nonlinear density contrast δ is to start from a Lagrangian region of linear density contrast $\delta_L = \mathcal{F}^{-1}(\delta)$, which obeys the spherical profile (25) and corresponds to the saddle-point of the action (23). As recalled in section 3, the path integral (22) is increasingly sharply peaked around this initial state at large mass scales, which explains why the dispersion of linear density contrasts δ_L measured in the simulations decreases with $\sigma(M)$. At smaller mass, one is sensitive to an increasingly broad region around the saddle-point, which mostly includes non-spherical initial fluctuations. Since these initial conditions are less efficient to concentrate matter in a small region one needs a larger linear density contrast δ_L to reach the same nonlinear threshold δ within the Eulerian radius r , which is why the distribution is not symmetric and mostly broadens by increasing its typical upper bound δ_L^+ . In principles, it may be possible to estimate the width of this distribution, at large masses, by expanding the action $\mathcal{S}[\delta_L]$ around its saddle-point.

We compare in Fig. 6 the prediction (34) (solid line labeled as $\delta_L = \mathcal{F}^{-1}(\delta)$) with results from numerical simulations, for the nonlinear threshold $\delta = 200$ at redshift $z = 0$. In our case, this corresponds to a linear density contrast $\delta_L \simeq 1.59$, that is obtained from Fig. 2 or the fit (12). As in section 3, we consider a Λ CDM cosmology with $(\Omega_{m0}, \Omega_{\Lambda0}, \sigma_8, n_s, h) = (0.27, 0.73, 0.79, 0.95, 0.7)$. This corresponds to the cosmological parameters of the largest-box numerical simulations of Tinker et al. (2008), which allow the best comparison with the theoretical predictions, as they also define halos by the density threshold $\delta = 200$ with a spherical-overdensity algorithm. The numerical results are the fits to the mass function given in Sheth & Tormen (1999) (“ST”), Jenkins et al. (2001) (“J”), Reed et al. (2003) (“R”), Warren et al. (2006) (“W”) and Tinker et al. (2008) (“T”). Note that these mass func-

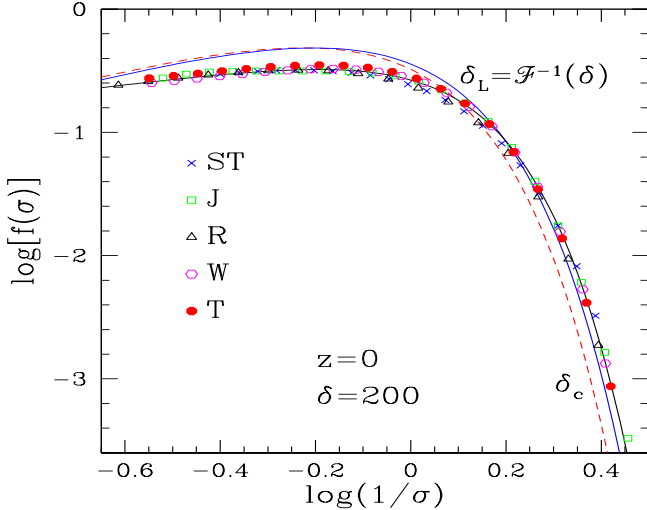


Fig. 6. The mass function at redshift $z = 0$ of halos defined by the nonlinear density contrast $\delta = 200$. The points are the fits to numerical simulations from Sheth & Tormen (1999), Jenkins et al. (2001), Reed et al. (2003), Warren et al. (2006) and Tinker et al. (2008). The dashed line (“ δ_c ”) is the usual Press-Schechter mass function, while the solid line that goes close to the Press-Schechter prediction at small mass is the mass function (34) with the exact cutoff (32). Here we have $\delta_L \simeq 1.59$. The second solid line that agrees with simulations over the whole range is the fit (36), that obeys the same large-mass exponential cutoff.

tions are defined in slightly different fashions, using either a spherical-overdensity or friends-of-friends algorithm, and density contrast thresholds that vary somewhat about $\delta = 200$. However, they agree rather well, as the dependence on δ is rather weak. This can be understood from Fig. 1, which shows that around $\delta = 200$ the linear density contrast $\delta_L = \mathcal{F}^{-1}(\delta)$ has a very weak dependence on δ . We also plot the usual Press-Schechter prediction (dashed line labeled δ_c), that amounts to replace δ_L by $\delta_c = 1.686$ in Eq.(34). We can see that using the exact value $\delta_L = \mathcal{F}^{-1}(\delta)$ significantly improves the agreement with numerical simulations at large masses. Note that there are no free parameters in Eq.(34). Of course, at small masses the mass function (34) closely follows the usual Press-Schechter prediction and shows the same level of disagreement with numerical simulations. This is expected since only the exponential cutoff (32) has been exactly derived from section 3. Since at large masses the power-law prefactor $1/\sigma$ in Eq.(34) is also unlikely to be correct, as discussed above, we give a simple fit that matches the numerical simulations from small to large masses (solid line that runs through the simulation points) while keeping the exact exponential cutoff:

$$f(\sigma) = 0.5 [(0.6\nu)^{2.5} + (0.62\nu)^{0.5}] e^{-\nu^2/2}, \quad (36)$$

with

$$\nu = \frac{\delta_L}{\sigma}, \quad \delta_L = \mathcal{F}^{-1}(\delta) \simeq 1.59 \text{ for } \delta = 200, \Omega_m = 0.27 \quad (37)$$

At higher redshift or for other Ω_m one simply needs to use the relevant mapping $\mathcal{F}^{-1}(\delta)$, shown in Fig. 2 or given by the simple fit (12) for $\delta = 200$. This mass function also

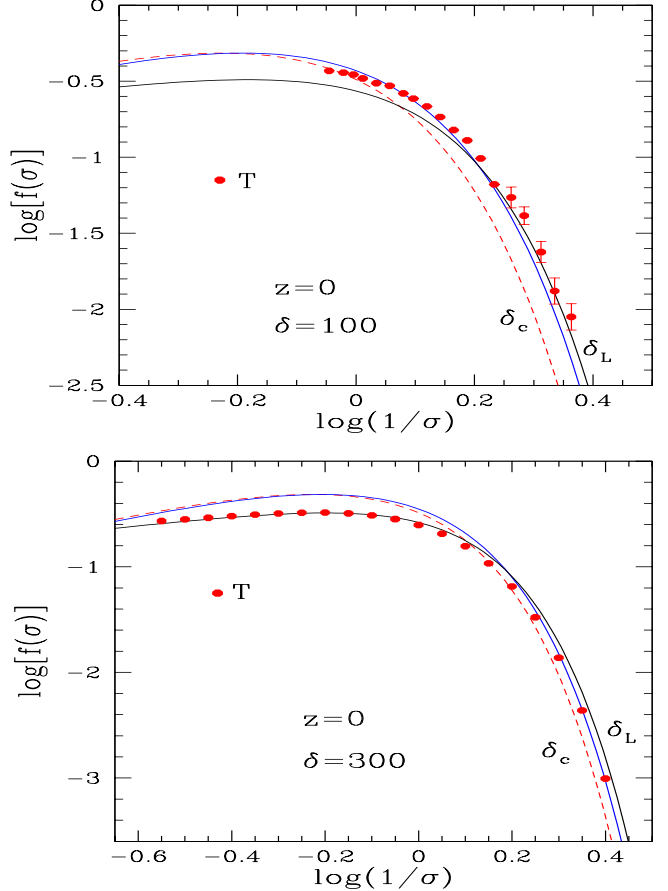


Fig. 7. The mass functions at $z = 0$ of halos defined by the nonlinear density contrasts $\delta = 100$ (upper panel) and $\delta = 300$ (lower panel). The points show the numerical simulations of Tinker et al. (2008). The dashed line is the usual Press-Schechter mass function, while the solid lines correspond to Eqs.(34) and (36), with now $\delta_L = \mathcal{F}^{-1}(100) \simeq 1.55$ (upper panel) and $\delta_L = \mathcal{F}^{-1}(300) \simeq 1.61$ (lower panel).

satisfies the normalization (35), whatever the value of the threshold δ_L .

Thus, we suggest that mass functions of virialized halos should be defined with a fixed nonlinear density threshold, such as $\delta = 200$, and fits to numerical simulations should use the exact exponential cutoff of Eq.(32), with the appropriate linear density contrast $\delta_L = \mathcal{F}^{-1}(\delta)$, rather than treating this as a free parameter. This would automatically ensure that the large mass tail has the right form (up to sub-leading terms such as power-law prefactors), as emphasized by the reasonable agreement with simulations of Eq.(34) at large masses. Moreover, it is best not to introduce unnecessary free parameters that become partly degenerate. Here we must note that Barkana (2004) had already noticed that, taking the spherical collapse at face value and defining halos by a nonlinear threshold δ (he chose $\delta = 18\pi^2$), one should use the linear threshold $\delta_L = \mathcal{F}^{-1}(\delta)$ for the Press-Schechter mass function. Unfortunately, noticing that the value of δ_L given by fits to numerical simulations was even lower, he concluded that this was not sufficient to reconcile theoretical predictions with numerical results. As shown by

Fig. 6, this is not the case, as the parameter δ_L used in fitting formulae is partly degenerate with the exponents of the power-law prefactors, so that it is possible to match numerical simulations while satisfying the large-mass tail (32). Of course, the actual justification of the asymptote (32) is provided by the analysis of section 3, which shows that below the upper bound δ_+ the spherical collapse is indeed relevant and asymptotically correct at large masses, as it corresponds to the saddle-point of the action (23).

Note that the result (32) also implies that the mass function $f(\sigma)$ is not exactly universal, since the mapping $\delta \mapsto \delta_L = \mathcal{F}^{-1}(\delta)$ shows a (very) weak dependence on cosmological parameters, see Fig. 2. Using the exact tail (32) should also improve the robustness of the mass function with respect to changes of cosmological parameters and redshifts.

Next, we compare in Fig. 7 the mass functions obtained at $z = 0$ for the density thresholds $\delta = 100$ and $\delta = 300$ with the numerical simulations from Tinker et al. (2008), who also considered these density thresholds. We show the usual Press-Schechter mass function (dashed line) and the results obtained from Eqs.(34) and (36) (solid lines), with now $\delta_L = \mathcal{F}^{-1}(100) \simeq 1.55$ and $\delta_L = \mathcal{F}^{-1}(300) \simeq 1.61$. We can see that the large mass tail remains consistent with the simulations, but for the case $\delta = 100$ it seems that the shape of the mass function at low and intermediate masses is modified and cannot be absorbed through the rescaling of δ_L . It appears to follow Eq.(34) rather than the fit (36), but this is likely to be a mere coincidence. We should note that Fig. 5 shows that $\delta_+ < 300$ for massive halos, so that shell-crossing should be taken into account and the tail (32) is no longer exact for $\delta = 300$, although it should still provide a reasonable approximation, as checked in Fig. 7. Thus, even though Tinker et al. (2008) also studied higher density thresholds, we do not consider such cases here as the tail (32) no longer applies.

5. Halo density profile

As for the mass function $n(M)$, the analysis of section 3 shows that the density profile of rare massive halos is given by the spherical saddle-point (25), see also Barkana (2004) and Prada et al. (2006). This holds for halos selected by some nonlinear density threshold δ in the limit of rare events, provided shell-crossing has not occurred beyond the associated radius r . In particular, this only applies to the outer part of the halo since in the inner part, at $r' \ll r$, shell-crossing must be taken into account. Then, as discussed in section 3, a strong radial-orbit instability comes into play and modifies the profile in this inner region, as deviations from spherical symmetry govern the dynamics and the virialization process (Valageas 2002b).

We compare in Fig. 8 the nonlinear density profile obtained from Eq.(25) with fits to numerical simulations. We plot the overdensity within radius r' , $1 + \delta_r = \rho_m(< r')/\bar{\rho}_m$, as a function of radius r . This is again obtained from Eq.(25) with the mapping $q'^3 = (1 + \delta_r)r'^3$ and $\delta_{r'} = \mathcal{F}(\delta_{Lq'})$. Since this only applies to the limit of rare events, we choose for each mass M a redshift z such that $\sigma(M, z) = 0.5$. Thus, smaller masses are associated with higher redshifts. The results do not significantly depend on the precise value of the criterium used to define rare events, here $\sigma(M, z) = 0.5$. The points in Fig. 8 are the results ob-

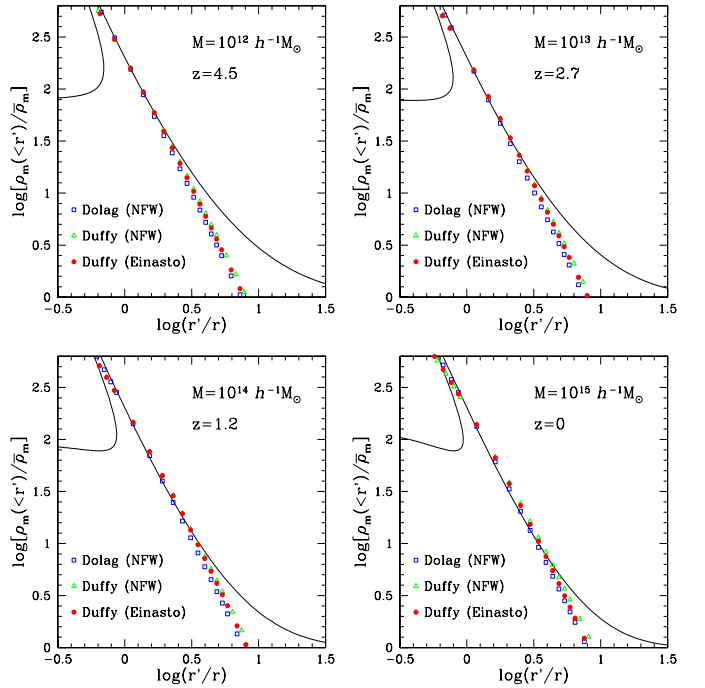


Fig. 8. The density profile of rare massive halos, for several masses M . For each mass the redshift is such that $\sigma(M, z) = 0.5$, as the theoretical prediction from Eq.(25) (solid line) only applies to rare events. The second branch that appears at small radii is due to the shell-crossing, hence the theoretical prediction only holds to the right of this branch. The points are fits to numerical simulations, based on an NFW profile (Dolag et al. 2004; Duffy et al. 2008) or an Einasto profile (Duffy et al. 2008). Note that we show the mean density within radius r' , $\rho_m(< r')/\bar{\rho}_m$, rather than the local density at radius r' , so that the NFW and Einasto profiles are integrated once.

tained from a Navarro, Frenk & White profile (Navarro et al. 1997, NFW),

$$\rho(r') = \frac{\rho_s}{(r'/r_s)(1 + r'/r_s)^2}, \quad (38)$$

or an Einasto profile (Einasto 1965),

$$\ln[\rho(r')/\rho_{-2}] = -\frac{2}{\alpha} [(r'/r_{-2})^\alpha - 1]. \quad (39)$$

For the NFW profile, the characteristic radius r_s is obtained from the concentration parameter, $c(M, z) = r/r_s$, where as in the previous sections r is the Eulerian radius where $\delta_r = 200$ (i.e. $r = r_{200}$). Then, we use in Fig. 8 the two fits obtained in Dolag et al. (2004) and Duffy et al. (2008) from numerical simulations, of the form $c(M, z) = a(M/M_0)^b(1+z)^c$. For the Einasto profile, we use the fits obtained in Duffy et al. (2008) for the concentration parameter, $c(M, z) = r/r_{-2}$, and for the exponent α (written as a quadratic polynomial over $\nu = \delta_c/\sigma(M, z)$ as in Gao et al. (2008)). Then, we integrate over r' the profiles (38)-(39), to obtain the overdensity profiles $\rho_m(< r')/\bar{\rho}_m$ shown in Fig. 8 (as $\rho_m(< r')$ is the mean density within radius r' and not the local density at radius r' as in Eqs.(38)-(39)).

We can check in Fig. 8 that our results agree reasonably well with these fits to numerical simulations over the range where both predictions are valid. Note that our prediction has no free parameter, since it is given by the saddle-point profile (25). At large radii we recover the mean density of the Universe, while the numerical profiles (38)-(39) go to zero, but this is an artefact of the forms (38)-(39), that were designed to give a sharp boundary for the halos and are mostly used for the high-density regions. For a study of numerical simulations at outer radii, see Figs.8 and 10 of Prada et al. (2006) which recover the mean density of the Universe at large scales. At small radii, the second branch that makes a turn somewhat below r is due to shell-crossing that makes the function $\rho_m(< r')$ bivariate. Below the maximum shell-crossing radius, for each Eulerian radius r' there are two Lagrangian radii q' , a large one that corresponds to shells that are still falling in, and a smaller one that corresponds to shells that have already gone once through the center (note that in agreement with Fig. 4, shell-crossing appears at slightly smaller relative radii for smaller mass). Then, the theoretical prediction only holds to the right of this second branch, where there is only one branch and no shell-crossing. Note that the theoretical prediction (25) explicitly shows that the halo density profiles are not universal. Within the phenomenological fits (38)-(39) this is parameterized through the dependence on mass and redshift of the concentration parameter and of the exponent α . However, we can see that over the regime where Eq.(25) applies the local slope of the halo density is $\rho(r') \sim r'^{-2}$, which explains the validity of the fits (38)-(39) in this domain. Unfortunately, our approach cannot shed light on the inner density profile, where $\delta_{r'} \gg 200$, which is the region of interest for most practical applications of the fits (38)-(39).

The same approach, based on the spherical collapse, was studied in greater details in Betancort-Rijo et al. (2006) and Prada et al. (2006). They consider the “typical” profile (25) that we study here, as well as “mean” and “most probable” profiles. In agreement with the steepest-descent approach of section 3, they find that the most probable profile closely follows the typical profile (25) and they obtain a good match with numerical simulations for massive halos, paying particular attention to outer radii. Therefore, we do not further discuss halo profiles here.

6. Halo bias

In addition to their multiplicity and their density profile, a key property of virialized halos is their two-point correlation function. At large scales it is usually proportional to the matter density correlation, up to a multiplicative factor b^2 , called the bias of the specific halo population. We revisit in this section the derivation of the bias of massive halos, following Kaiser (1984), and we point out that paying attention to some details it is possible to reconcile the theoretical predictions with numerical simulations, without introducing any free parameter.

As seen in the previous sections, rare massive halos can be identified with rare spherical fluctuations in the initial (linear) density field. More precisely, as in section 3 we may consider the bivariate density distribution, $\mathcal{P}(\delta_{r_1}, \delta_{r_2})$, of the density contrasts $\delta_{r_1}, \delta_{r_2}$, in the spheres of radii r_1, r_2 , centered at points $\mathbf{x}_1, \mathbf{x}_2$. Thus, we introduce as in Eq.(19)

the double Laplace transform $\varphi(y_1, y_2)$,

$$e^{-\varphi(y_1, y_2)/\sigma^2} = \langle e^{-(y_1 \delta_{r_1} + y_2 \delta_{r_2})/\sigma^2} \rangle \\ = \int_{-1}^{\infty} d\delta_{r_1} d\delta_{r_2} e^{-(y_1 \delta_{r_1} + y_2 \delta_{r_2})/\sigma^2} \mathcal{P}(\delta_{r_1}, \delta_{r_2}), \quad (40)$$

where $\sigma^2 = \sigma_{r,r}^2(0)$ is the linear variance (18) at some scale r . If $r_1 = r_2$ we may take $r = r_1 = r_2$, otherwise it can be any intermediate scale, as the results do not depend on this factor. The only requirement is that σ should scale as σ_{r_1} and σ_{r_2} , which is obtained by choosing for instance a fixed ratio $r/\sqrt{r_1 r_2}$. Then, the probability distribution $\mathcal{P}(\delta_{r_1}, \delta_{r_2})$ can be obtained from the cumulant generating function $\varphi(y_1, y_2)$ through a double inverse Laplace transform, as in Eq.(20). Next, $\varphi(y_1, y_2)$ can be written in terms of the linear density field as a path integral, such as (22), with an action that now reads as

$$\mathcal{S}[\delta_L] = y_1 \delta_{r_1}[\delta_L] + y_2 \delta_{r_2}[\delta_L] + \frac{\sigma^2}{2} \delta_L \cdot C_L^{-1} \cdot \delta_L \quad (41)$$

Then, for rare events the tail of the distribution $\mathcal{P}(\delta_{r_1}, \delta_{r_2})$ is governed by the last Gaussian weight of (41), as in Eq.(30),

$$\sigma \rightarrow 0 : \mathcal{P}(\delta_{r_1}, \delta_{r_2}) \sim e^{-\frac{1}{2} \delta_L \cdot C_L^{-1} \cdot \delta_L}, \quad (42)$$

where $\delta_L[\mathbf{q}]$ is the relevant saddle-point of the action \mathcal{S} . Unfortunately, since the action (41) is no longer spherically symmetric, it is not possible to obtain an explicit expression of its minimum. Therefore, we must rely on some simple approximations. In the limit of large distance, $x_{12} = |\mathbf{x}_2 - \mathbf{x}_1| \rightarrow \infty$, between the positions of both halos, the linear field $\delta_L(\mathbf{s})$ around the Lagrangian positions $\mathbf{s}_1, \mathbf{s}_2$, of the halos should follow the profile (25) (we note the Lagrangian coordinates \mathbf{s}_i to avoid confusion with the Lagrangian radii q_i). Thus, we neglect the tidal forces of the halos, but we keep track of the mean displacement of each halo, due to the gravitational attraction from the other one, by distinguishing their Lagrangian positions $\mathbf{s}_1, \mathbf{s}_2$, from their Eulerian positions $\mathbf{x}_1, \mathbf{x}_2$. Within this approximation, the distribution $\mathcal{P}(\delta_{r_1}, \delta_{r_2})$ can be estimated from the Gaussian distribution $\mathcal{P}_L(\delta_{Lq_1}, \delta_{Lq_2})$ of the linear density contrasts $\delta_{Lq_1}, \delta_{Lq_2}$, at positions $\mathbf{s}_1, \mathbf{s}_2$, within the Lagrangian spheres of radii q_1 and q_2 , with the mapping (26). This closely follows the approach introduced in Kaiser (1984), except for the distinction between \mathbf{s}_i and \mathbf{x}_i . The joint distribution $\mathcal{P}_L(\delta_{Lq_1}, \delta_{Lq_2})$ reads as (see also Kaiser 1984; Politzer & Wise 1984)

$$\mathcal{P}_L(\delta_{Lq_1}, \delta_{Lq_2}) = \frac{1}{(2\pi)\sqrt{\det M}} e^{-\frac{1}{2} \sum_{i,j} \delta_{Lq_i} \cdot M_{ij}^{-1} \cdot \delta_{Lq_j}}, \quad (43)$$

where M is the linear covariance matrix,

$$M = \begin{pmatrix} \sigma_1^2 & \sigma_{12}^2 \\ \sigma_{12}^2 & \sigma_2^2 \end{pmatrix}. \quad (44)$$

Here we defined from Eq.(18), $\sigma_i^2 = \sigma_{q_i, q_i}^2(0)$ and $\sigma_{12}^2 = \sigma_{q_1, q_2}^2(s_{12})$ with $s_{12} = |\mathbf{s}_2 - \mathbf{s}_1|$. The inverse of the matrix M writes as

$$M^{-1} = \frac{1}{\sigma_1^2 \sigma_2^2 - \sigma_{12}^4} \begin{pmatrix} \sigma_2^2 & -\sigma_{12}^2 \\ -\sigma_{12}^2 & \sigma_1^2 \end{pmatrix}. \quad (45)$$

This yields

$$\mathcal{P}_L(\delta_{Lq_1}, \delta_{Lq_2}) = \mathcal{P}_L(\delta_{Lq_1}) \mathcal{P}_L(\delta_{Lq_2}) \frac{\sigma_1 \sigma_2}{\sqrt{\sigma_1^2 \sigma_2^2 - \sigma_{12}^4}} \\ \times \exp \left[\frac{2\delta_{Lq_1} \delta_{Lq_2} \sigma_{12}^2 - \delta_{Lq_1}^2 \sigma_{12}^4 / \sigma_1^2 - \delta_{Lq_2}^2 \sigma_{12}^4 / \sigma_2^2}{2(\sigma_1^2 \sigma_2^2 - \sigma_{12}^4)} \right]. \quad (46)$$

Next, defining the real-space halo correlation $\xi_{M_1, M_2}(r)$ as the fractional excess of halo pairs (Kaiser 1984; Peebles 1980),

$$n_{\mathbf{x}_1, \mathbf{x}_2}(M_1, M_2) dM_1 dM_2 d\mathbf{x}_1 d\mathbf{x}_2 = \\ \bar{n}(M_1) \bar{n}(M_2) (1 + \xi_{M_1, M_2}(x_{12})) dM_1 dM_2 d\mathbf{x}_1 d\mathbf{x}_2, \quad (47)$$

which also gives the conditional probability,

$$n_{\mathbf{x}_1, \mathbf{x}_2}(M_2 | M_1) = \bar{n}(M_2) (1 + \xi_{M_1, M_2}(x_{12})), \quad (48)$$

we write

$$1 + \xi_{M_1, M_2}(x_{12}) \sim (1 + \delta_M(x_{12})) \frac{\mathcal{P}_L(\delta_{L1}, \delta_{L2})}{\mathcal{P}_L(\delta_{L1}) \mathcal{P}_L(\delta_{L2})}, \quad (49)$$

where the mass of each halo is given by $M_i = \bar{\rho}_m 4\pi q_i^3 / 3$ and $\delta_{Li} = \mathcal{F}^{-1}(\delta_i)$ are the linear density contrasts which are associated with the nonlinear density contrasts δ_i that define the halos, as in section 4 and Fig. 2. In Eq.(49) the factor $(1 + \delta_M(x_{12}))$ models the effects associated with the mapping from Lagrangian to Eulerian space. Indeed, in the limit of rare massive halos and large separation, the number of neighbors is conserved and we write $n_{\text{Eul}} x_{12}^2 dx_{12} = n_{\text{Lag}} s_{12}^2 ds_{12}$ (for an integral form of the conservation of pairs, or neighbors, see Peebles 1980). We take $ds_{12} = (1 + \delta_M) d\mathbf{x}_{12}$, where we define $\delta_M(x_{12})$ as the local nonlinear density contrast at Eulerian distance x_{12} from a halo of mass M , obtained from the profile (25), and we choose $M = \max(M_1, M_2)$ (which obeys the symmetry $M_1 \leftrightarrow M_2$), whence $q = \max(q_1, q_2)$. This reflects the fact that the gravitational attraction of a massive halo pulls matter towards it center with a strength that depends on distance, so that the Jacobian $|\partial \mathbf{q} / \partial \mathbf{x}| = (1 + \delta)$ is different from unity. In a sense this is a tidal effect, as a locally volume-preserving displacement would not affect the number densities, which is why we take for $\delta_M(x_{12})$ the density contrast at distance x_{12} and not the density contrast within radius x_{12} . We may note that a local bias model (Mo & White 1996), using a peak-background split argument (Efstathiou et al. 1988), would rather give a quadratic factor $(1 + \delta_1)(1 + \delta_2)$. However, we prefer to keep the linear factor (49) as it also remains consistent in case of large displacements². This also expresses the fact that all pairs cannot simultaneously get closer (as fluctuations grow some objects move closer but they also further separate from other emerging groups). Then, defining the halo bias as

$$b_{M_1, M_2}^2(r) = \frac{\xi_{M_1, M_2}(r)}{\xi(r)}, \quad (50)$$

where $r = x_{12}$ and $\xi(r)$ is the nonlinear matter correlation, we obtain the bias from Eq.(49). Note that the bias (50)

² For instance, let us consider a large system which can be subdivided into cells of two classes, $\{+, -\}$, with matter densities $\{\rho_+, \rho_-\}$ and volume fractions $\{\eta_+, \eta_-\}$, and $\rho_+ > \bar{\rho} > \rho_-$, $\eta_+ < \eta_-$. Then, from the conservation of volume ($\eta_+ + \eta_- = 1$) and mass ($\eta_+ \rho_+ + \eta_- \rho_- = \bar{\rho}$), we obtain in the limits $\rho_+ \gg 1$ and $\rho_- \ll 1$, $\xi = \langle \rho^2 \rangle_c / \bar{\rho}^2 \sim \rho_+ / \bar{\rho}$.

does not factorize, $b_{M_1, M_2}^2(r) \neq b_{M_1}(r) b_{M_2}(r)$, because of the terms σ_{12} and δ_M .

At large separation, $r \rightarrow \infty$, we are in the linear regime, so that the matter correlation reads as $\xi(r) \simeq \sigma_{0,0}^2(r)$, and the local density contrast $\delta_M(r)$ is small and close to the linear density contrast $\delta_L(s)$. Note that this is the density contrast at Lagrangian radius s , and not the mean density contrast within radius s . Therefore, it is related to Eq.(25) by

$$3q^2 \delta_L(q) = \frac{\partial}{\partial q} (q^3 \delta_{Lq}), \quad (51)$$

whence

$$\delta_L(s) = \delta_L \frac{\tilde{\sigma}^2(q, s)}{\sigma_q^2}, \quad (52)$$

with $\delta_L = \mathcal{F}^{-1}(200)$ for instance, and using Eq.(18)

$$\tilde{\sigma}^2(q, s) = 4\pi \int dk k^2 P_L(k) W(kq) \frac{\sin(ks)}{ks} = \sigma_{q,0}^2(s). \quad (53)$$

Then, from Eq.(50), the bias of halos defined by the same linear threshold, $\delta_L = \mathcal{F}^{-1}(\delta)$, reads as

$$b_{M_1, M_2}^2(r) = \frac{1}{\sigma_{0,0}^2(r)} \left[-1 + \frac{\sigma_{q_1} \sigma_{q_2} (1 + \delta_L \sigma_{q,0}^2(s) / \sigma_q^2)}{\sqrt{\sigma_{q_1}^2 \sigma_{q_2}^2 - \sigma_{q_1, q_2}^4(s)}} \right] \\ \times \exp \left(\frac{2\delta_L^2 \sigma_{q_1, q_2}^2(s) - \delta_L^2 \sigma_{q_1, q_2}^4(s) / \sigma_{q_1}^2 - \delta_L^2 \sigma_{q_1, q_2}^4(s) / \sigma_{q_2}^2}{2[\sigma_{q_1}^2 \sigma_{q_2}^2 - \sigma_{q_1, q_2}^4(s)]} \right). \quad (54)$$

For equal-mass halos this simplifies as

$$b_M^2(r) = \frac{1}{\sigma_{0,0}^2(r)} \left[-1 + \left(1 + \delta_L \frac{\sigma_{q,0}^2(s)}{\sigma_q^2} \right) \frac{\sigma_q^2}{\sqrt{\sigma_q^4 - \sigma_{q,q}^4(s)}} \right] \\ \times \exp \left(\frac{\delta_L^2 \sigma_{q,q}^2(s) - \delta_L^2 \sigma_{q,q}^4(s) / \sigma_q^2}{\sigma_q^4 - \sigma_{q,q}^4(s)} \right). \quad (55)$$

Note that the argument of the exponential is not necessarily small, as stressed in Politzer & Wise (1984). Indeed, we only assumed a large separation limit, i.e. $\sigma_{q,q}^2(s) \ll \sigma_q^2$, and a rare-event limit, $\delta_L / \sigma_q \gg 1$. Thus, at fixed (small) ratio $\sigma_{q,q}^2(s) / \sigma_q^2$, we obtain a large exponent in the limit of large-mass halos, $\sigma_q^2 \rightarrow 0$. Then, keeping the full expressions (54) or (55) gives a nonlinear bias, since $b_M^2(r)$ is not a simple number and shows a non-trivial scale dependence, as will be clearly seen in Fig. 11 below. Indeed, these results cannot be recovered through a linear biasing scheme, where the fluctuations of the halo number density field, $\delta_{\text{halo}} = (n - \bar{n}) / \bar{n}$, are written as $\delta_{\text{halo}}(M) = b(M) \delta_R$ (where the matter density field is smoothed over some larger scale R), which would lead to $\xi_M(r) \propto \sigma_{R,R}^2(r)$ whereas Eqs.(54)-(55) generate powers of all orders over $\sigma_{q,q}^2(r)$. In the local bias framework (Fry & Gaztanaga 1993; Mo et al. 1997), where one writes $\delta_{\text{halo}}(M) = \sum_i b_i(M) \delta_R^i$, this could be interpreted as non-zero bias coefficients b_i for $i \geq 2$. However, Eqs.(54)-(55) are not equivalent to such a local model, inspired from a peak-background split argument (Efstathiou et al. 1988). Indeed, they do not involve

any external smoothing scale R and they depend on the three linear correlations $\sigma_{0,0}^2(r)$, $\sigma_{q,0}^2(r)$ and $\sigma_{q,q}^2(r)$.

Finally, we must express the Lagrangian separation s in terms of the Eulerian distance r . At lowest order we again consider each halo as a test particle that falls into the potential well built by the other halo (i.e. we neglect backreaction effects). Then, from the analysis of section 3 and the linear profile (25), we know that a test particle at Lagrangian distance q' from one halo has moved to position r' , according to the mapping (26). Using Eq.(25) this gives at first order

$$q' \simeq r' \left(1 + \frac{\delta_{r'}}{3} \right) \simeq r' \left(1 + \frac{\delta_{Lq'}}{3} \right), \quad (56)$$

since at large distance we have $\delta_{r'} \simeq \delta_{Lq'} \ll 1$. Therefore, we obtain the Lagrangian separation s as the solution of the implicit equation

$$r = s \left(1 - \frac{\delta_L}{3} \frac{\sigma_{q_1,s}^2}{\sigma_{q_1}^2} - \frac{\delta_L}{3} \frac{\sigma_{q_2,s}^2}{\sigma_{q_2}^2} \right), \quad (57)$$

where again we only kept the first-order term and we took into account the displacements of both halos. Together with Eq.(54), or Eq.(55), this defines our prediction for the bias of massive collapsed halos. Note that this approach also applies to the cross-correlation between different redshifts.

At large separation, $r \rightarrow \infty$, and fixed mass (i.e. fixed σ_q), we may linearize the bias (55) over $\sigma^2(s)$ as

$$r \rightarrow \infty : b_M^2(r) \sim \frac{1}{\sigma_{0,0}^2(r)} \left[\delta_L \frac{\sigma_{q,0}^2(s)}{\sigma_q^2} + \delta_L^2 \frac{\sigma_{q,q}^2(s)}{\sigma_q^4} \right]. \quad (58)$$

For large masses, where $\sigma_q \ll 1$, but not too large, so that the exponent in (55) is still small, this gives

$$r \rightarrow \infty, M \rightarrow \infty : b_M(r) \sim \frac{\delta_L}{\sigma_q^2} \frac{\sigma_{q,q}(s)}{\sigma_{0,0}(r)}. \quad (59)$$

Thus we recover the result of Kaiser (1984) and Mo & White (1996), except for the multiplicative factor $\sigma_{q,q}(s)/\sigma_{0,0}(r)$. It expresses the facts that halos only probe the linear density field smoothed over the Lagrangian scale q (i.e. the formation of a halo does not depend on wavelengths much smaller than its radius) and that halos have moved from distance s to r by their mutual gravitational attraction. This factor yields a weak scale dependence for $b(M)$, as the slope of the linear power spectrum slowly varies with scale r . We can also note that at lowest order over $\sigma^2(s)$ we may write the solution of Eq.(57) as

$$s = r \left(1 + \frac{\delta_L}{3} \frac{\sigma_{q_1,r}^2}{\sigma_{q_1}^2} + \frac{\delta_L}{3} \frac{\sigma_{q_2,r}^2}{\sigma_{q_2}^2} \right), \quad (60)$$

which provides a simple explicit expression for s .

We compare in Figs. 9-11 the bias obtained from Eqs. (55), (57), with fits to numerical simulations. We first show in Fig. 9 our prediction as a function of halo mass, at redshift $z = 0$ and distance $r = 50h^{-1}$ Mpc. This is typically the scale that is considered in numerical simulations to compute the large-scale bias, as $b(r)$ is expected to be almost constant at large scales (Kaiser 1984; Mo & White 1996), see also Eq.(59). We also plot the standard theoretical prediction from Mo & White (1996) (dashed line). We

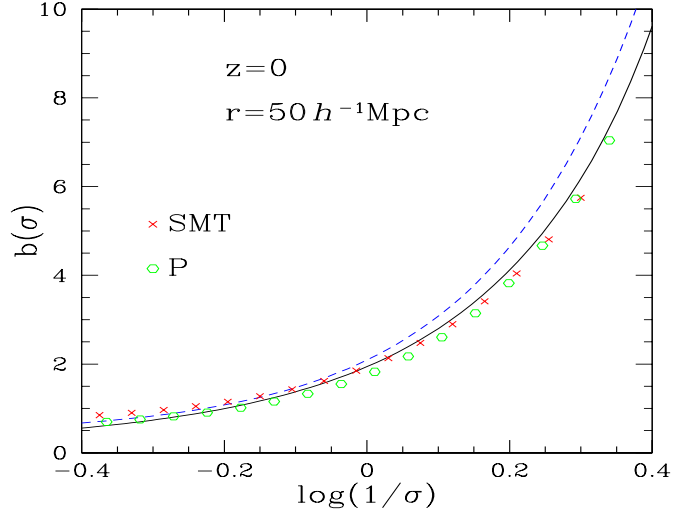


Fig. 9. The halo bias $b(\sigma)$, as a function of $\sigma(M)$, at redshift $z = 0$ and distance $r = 50h^{-1}$ Mpc. The solid line is the theoretical prediction (55)-(57), and the dashed line is the bias obtained in Mo & White (1996). The points are the fits to numerical simulations, from Sheth, Mo & Tormen (2001) (crosses) and Pillepich (2009) (circles).

can see that our result (55)-(57) agrees rather well with numerical simulations and the popular fit from Sheth, Mo & Tormen (2001). As expected, it follows the trend of the prediction from Mo & White (1996), since both derivations follow the spirit of Kaiser (1984) (i.e. one identifies halos from overdensities in the linear density field) and they agree at large scale for rare massive halos, up to a factor of order unity, as seen in Eq.(59). Note that Eqs. (55)-(57) only apply to the rare-event limit, as for small objects the approximations used in the derivation no longer apply. In particular, halos can no longer be considered as spherical isolated objects, and one should take into account merging effects. Note that this caveat also applies to other analytical approaches, such as Kaiser (1984) and Mo & White (1996). Then, our prediction should only be used for large masses, for instance such that $b > 1$.

Next, we compare in Fig. 10 the dependence on r of the bias (55)-(57) with the fit to numerical simulations from Hamana et al. (2001) (using their cosmological parameters). The crosses are the large-scale limit given by Sheth, Mo & Tormen (2001) and we only plot our prediction (solid lines) down to scale $r = 2q$, since it should only apply to large halo separations. We can see that the scale-dependence that we obtain is opposite to the one observed in the simulations. However, both are very weak and the prediction (55)-(57) may still lie within error bars of numerical results. For the largest mass, $M = 10^{15}h^{-1}M_\odot$, we also plot for illustration the linearized bias (58) (lower dashed line), and the non-linear bias (55) where we set $s = r$ (upper dot-dashed line) or we use Eq.(60) (lower dotted line). As expected, at very large scales the linearized bias (58) agrees with the non-linear expression (55). Using the simpler Eq.(60) also gives the same results at large scales, but the Lagrangian to Eulerian mapping still gives a non-negligible correction as shown by the upper dot-dashed line where we set $s = r$. In any case, it is always best to use the full expression (55)-(57).

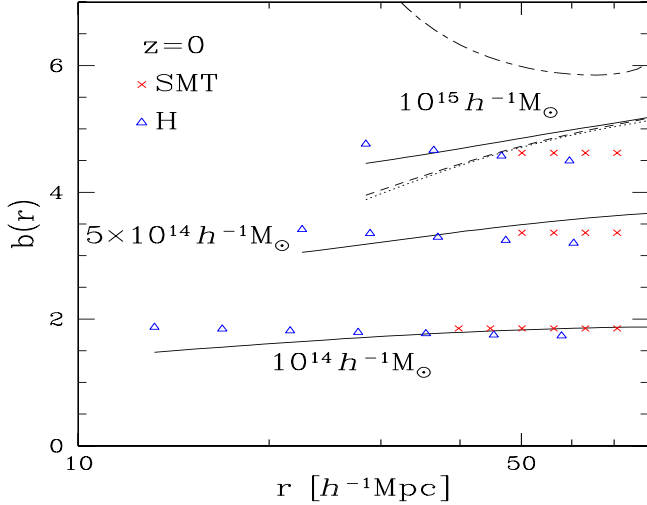


Fig. 10. The halo bias $b(r)$, as a function of scale r , at redshift $z = 0$ and for several masses. The solid line is the theoretical prediction (55)-(57). The crosses show the large-scale fit to numerical simulations from Sheth, Mo & Tormen (2001), while the triangles show the fit from Hamana et al. (2001). The dashed line is the linearized bias (58), the dot-dashed line is the nonlinear bias (55) where we set $s = r$ while the dotted line uses Eq.(60) (for $M = 10^{15} h^{-1} M_{\odot}$ in the three cases). We only plot our predictions for $r \geq 2q$.

We compare in Fig. 11 our results at high redshift, $z = 10$, with the fit to numerical simulations from Reed et al. (2009) (using their cosmological parameters). Again, the crosses are the large-scale limit of Sheth, Mo & Tormen (2001) and we only plot our prediction (solid lines) down to scale $r = 2q$. For $M = 10^{11} h^{-1} M_{\odot}$ we also plot the linearized bias (58) (lower dashed line), and the nonlinear bias (55) where we set $s = r$ (upper dot-dashed line) or we use Eq.(60) (dotted line). As noticed in Reed et al. (2009), the scale-dependence is much steeper than the one found at small redshifts and it is not consistent with the fits obtained at low z in Hamana et al. (2001) or Diaferio et al. (2003). This was interpreted as a breakdown of universality for massive halos at high redshift by Reed et al. (2009). However, we can see that our prediction (55)-(57) agrees reasonably well with their numerical results. Therefore, the change of behavior of the bias $b(r)$ between the two regimes studied in Figs. 10 and 11 can be understood from the standard picture of massive halos arising from rare overdensities in the initial (linear) Gaussian density field, by using the same theoretical prediction (55)-(57) that applies to any z . We can note that the linearized bias (58), or the approximation $s = r$, show strong deviations in this regime and disagree with the simulations. Therefore, one should use the nonlinear bias (55)-(57) (but using Eq.(60) gives similar results) and one cannot neglect the correction due to the Lagrangian to Eulerian mapping that is associated with $s \mapsto r$.

On the other hand, the comparison with the result from (58) shows that the steep dependence on scale is due to the nonlinear term in (55), i.e. keeping the exponential factor. Indeed, as noticed below Eq.(55), and in Politzer & Wise (1984), the derivation of the bias presented above only as-

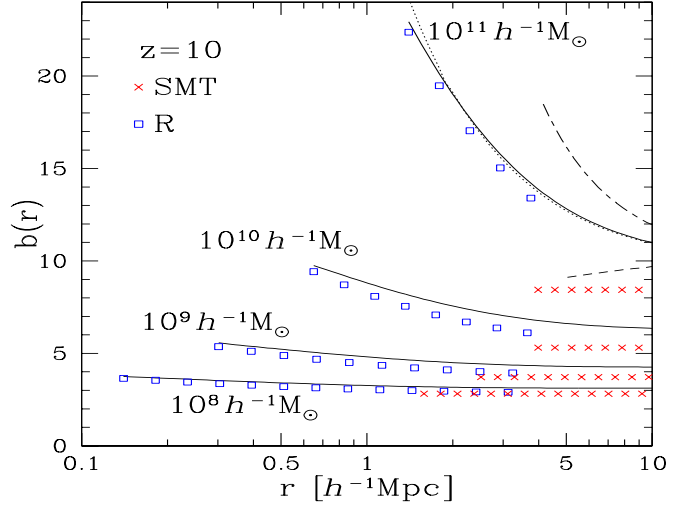


Fig. 11. The halo bias $b(r)$, as a function of scale r , at redshift $z = 10$ and for several masses. As in Fig. 10, the solid line is the prediction (55)-(57), while the crosses show the large-scale fit from Sheth, Mo & Tormen (2001), but the squares now show the fit to numerical simulations from Reed et al. (2009). The dashed line is the linearized bias (58), the dot-dashed line is the nonlinear bias (55) where we set $s = r$ while the dotted line uses Eq.(60) (for $M = 10^{11} h^{-1} M_{\odot}$ in the three cases). Again we only plot our predictions for $r \geq 2q$.

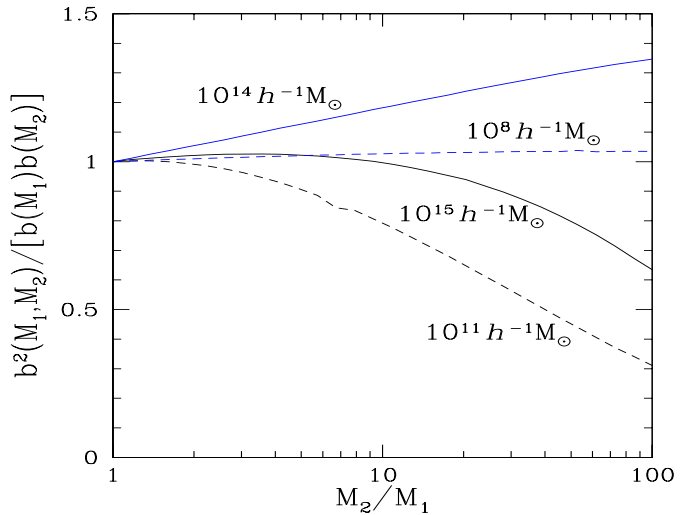


Fig. 12. The ratio $b^2(M_1, M_2)/[b(M_1)b(M_2)]$, from Eqs.(54) and (55), at fixed geometrical mean $M = \sqrt{M_1 M_2}$. Solid lines are for distance and redshift $(r, z) = (50 h^{-1} \text{Mpc}, 0)$, whereas dashed lines are for $(r, z) = (3 h^{-1} \text{Mpc}, 10)$. Curves are labelled by their fixed geometrical mean M .

sumes a large separation between very massive (rare) halos, that is, $\sigma_{q,q}^2(s) \ll \sigma_q^2$ and $\delta_L/\sigma_q \gg 1$. Therefore, for sufficiently massive objects (that correspond to a large bias), the variance σ_q^2 can be small enough to make the exponent in Eq.(55) of order unity or larger. Then, one needs to

keep the nonlinear expression (55) rather than expanding the exponential as in Eq.(58). As noticed below Eq.(55), this implies a nonlinear biasing scheme as the halo correlation is not proportional to the matter correlation but shows a steeper scale dependence. Within the local bias framework (Fry & Gaztanaga 1993; Mo et al. 1997), this could be interpreted as non-zero higher order bias parameters b_i in the expansion $\delta_{\text{halo}}(M) = \sum_i b_i(M)\delta_R^i$. However, the bias (55) cannot be exactly reduced to such a model (but one could certainly derive within such a framework a good approximation to Eq.(55), restricted to some larger scale R , by using Eq.(60), writing the correlations $\sigma_{q,0}^2(r)$ and $\sigma_{q,q}^2(r)$ in terms of $\sigma_{0,0}^2(r)$, expanding over $\sigma_{0,0}^2(r)$ and finally smoothing over the external scale R of interest).

We should stress here that our prediction (55)-(57) has no free parameter. This can lead to a slightly larger inaccuracy as compared with fits to simulations in the regime where the latter have been tested, as in Fig. 10, but this improves the robustness of the predictions as one consider other regimes (e.g. other cosmological parameters or other redshifts as in Fig. 11). Therefore, we think that Eqs.(55)-(57) could provide a useful alternative to current fitting formulae, as they can be readily applied to any set of cosmological parameters or redshifts.

Finally, we show in Fig. 12 the bias ratio $b^2(M_1, M_2)/[b(M_1)b(M_2)]$, as a function of the mass ratio M_2/M_1 , at fixed geometrical mean $M = \sqrt{M_1 M_2}$. We consider several mass scales M , at distance and redshift $(r, z) = (50h^{-1}\text{Mpc}, 0)$ (solid lines) and $(r, z) = (3h^{-1}\text{Mpc}, 10)$ (dashed lines). This shows that making the factorized approximation, $b^2(M_1, M_2) \simeq b(M_1)b(M_2)$, can lead to an error of up to 50% for a mass ratio $M_2/M_1 \sim 100$. Therefore, it is best to use the full Eq.(54).

7. Conclusion

We have pointed out in this article that the large-mass exponential tail of the mass function of collapsed halos is exactly known, provided halos are defined as spherical overdensities above a nonlinear density contrast threshold δ (i.e. using a spherical overdensity algorithm in terms of numerical simulations). This arises from the fact that massive rare events are governed by (almost) spherical fluctuations in the initial (linear) Gaussian density field (if one does not explicitly breaks statistical isotropy by looking for non-spherical quantities). This is most easily seen from a steepest-descent approach, which becomes asymptotically exact in the large-scale limit, applied to the action \mathcal{S} associated with the probability distribution of the nonlinear density contrast within spherical cells. This result holds for any nonlinear threshold δ used to define halos, provided it is below an upper bound δ_+ that marks the point where shell-crossing comes into play. For a standard Λ CDM cosmology, δ_+ typically grows from 200 to 600 as one goes from $10^{15}h^{-1}M_\odot$ to $10^{11}h^{-1}M_\odot$ (which also corresponds to increasing redshift). This dependence on mass is due to the change of slope of the linear power spectrum with scale.

We have also noted that in two similar systems, the one-dimensional adhesion models with Brownian or white-noise initial (linear) velocity, the same method can be used for both the density distribution $\mathcal{P}(\delta_r)$ and the mass function $n(M)$, and one can check that this yields rare-event tails

that agree with the exact distributions, which can be derived by other techniques (Valageas 2009a,b).

Therefore, defining collapsed halos by a threshold $\delta = 200$ to follow the common practice, the large-mass tail of the halo mass function is of the form $e^{-\delta_L^2/(2\sigma^2(M))}$, up to subleading prefactors such as power laws, where $\delta_L = \mathcal{F}^{-1}(\delta)$ is the linear density contrast associated to δ through the spherical collapse dynamics. In particular, we obtain $\delta_L \simeq 1.59$ for $\delta = 200$. We checked that this value, which is slightly lower than the commonly used value of $\delta_c = 1.686$ associated with complete collapse, gives a good match with numerical simulations (at large masses) when we simply use the Press-Schechter functional form. We also give a fitting formula, which obeys this exact exponential cutoff, that agrees with simulations over all mass scales.

We suggest that halos should be defined by such a nonlinear density threshold (i.e. friends-of-friends algorithms are not so clearly related to theoretical computations) and fits to numerical simulations should use this exact exponential tail, rather than treating δ_L as a free parameter. This would avoid introducing unnecessary degeneracies between fitting parameters and it would make the fits more robust.

Next, we have briefly recalled that in the large-mass limit the outer density profile of collapsed halos is given by the radial profile of the relevant spherical saddle-point. This applies to radii beyond the density threshold δ_+ , where shell-crossing comes into play. In agreement with numerical simulations, for rare massive halos this separates an outer region dominated by a radial flow from an inner region where virialization takes place and a strong transverse velocity dispersion quickly builds up. We have recalled that this can be explained from a strong radial-orbit instability, which implies that infinitesimal deviations from spherical symmetry are sufficient to govern the dynamics.

Finally, following the approach of Kaiser (1984), we have obtained an analytical formula for the bias of massive halos that improves the match with numerical simulations. In particular, it captures the steepening of the scale dependence that is observed for large-mass halos at higher redshifts. This requires keeping the bias in its nonlinear form and taking care of the Lagrangian-Eulerian mapping. We also note that using a factorization approximation, $b^2(M_1, M_2) \simeq b(M_1)b(M_2)$, may lead to non-negligible inaccuracies. We stress that this analytical estimate of the bias contains no free parameter. Although this can yield a match to numerical simulations that is not as good as fitting formulae derived from the same set of simulations, it provides a more robust prediction for general cases, as shown by the good agreement obtained at both low and high redshifts ($z = 0$ and $z = 10$), whereas published fitting formulae cannot reproduce both cases. We think this makes such a model useful for cosmological purposes, where it is desirable to have versatile analytical estimates that follow the correct trends as one varies cosmological parameters or redshifts. In particular, the scale-dependence of the bias of massive halos has recently been proposed as a test of primordial non-Gaussianity (e.g., Dalal et al. 2008), which requires robust theoretical models.

Our results are exact (for the mass function) or are expected to provide a good approximation (for the bias) in the limit of rare massive halos. However, this remains of interest as large-mass tails are also the most sensitive to cosmological parameters (e.g., through the linear growth factor and the primordial power spectrum), thanks to their

steep dependence on mass or scale. Moreover, we think that more general fitting formulae (such as the one we provide for the mass function) should follow such theoretical predictions in their relevant limits, so as to reduce the number of free parameters and improve their robustness.

References

- Bardeen J., Bond J.R., Kaiser N., Szalay A.S., 1986, *ApJ*, 304, 15
- Barkana R., 2004, *MNRAS*, 347, 59
- Bernardeau F., 1994a, *ApJ*, 427, 51
- Bernardeau F., 1994b, *A&A*, 291, 697
- Bernardeau F., Colombi S., Gaztanaga E., Scoccimarro R., 2002, *Phys. Rept.*, 367, 1
- Betancort-Rijo J.E., Montero-Dorta A.D., 2006, *ApJ*, 650, L95
- Betancort-Rijo J.E., Sanchez-Conde M.A., Prada F., Patiri S.G., 2006, *ApJ*, 649, 579
- Bond J.R., Cole S., Efstathiou G., Kaiser N., 1991, *ApJ*, 379, 440
- Bond J.R., Myers S.T., 1996, *ApJS*, 103, 1
- Borgani S., Rosati P., Tozzi P., et al., 2001, *ApJ*, 561, 13
- Cuesta A.J., Prada F., Klypin A., Moles M., 2008, *MNRAS*, 389, 385
- Dalal N., Dore O., Huterer D., Shirokov A., 2008, *Phys. Rev. D*, 77, 123514
- Diaferio A., Nusser A., Yoshida N., Sunyaev R., 2003, *MNRAS*, 338, 433
- Dolag K., Bartelmann M., Perrotta F., et al., 2004, *A&A*, 416, 853
- Duffy A. R., Schaye J., Kay S. T., Dalla Vecchia C., 2008, *MNRAS*, 390, L64
- Efstathiou G., Frenk C.S., White S.D.M., Davis M., 1988, *MNRAS*, 235, 715
- Einasto J., 1965, *Alma-Ata*, 51, 87
- Evrard A.E., 1989, *ApJ*, 341, L71
- Fry J.N., Gaztanaga E., 1993, *ApJ*, 413, 447
- Gao L., Navarro J., Cole S., et al., 2008, *MNRAS*, 387, 536
- Gurbatov S.N., Saichev A.I., Shandarin S.F., 1989, *MNRAS*, 236, 385
- Hamana T., Yoshida N., Suto Y., Evrard A.E., 2001, *ApJ*, 561, L143
- Jenkins A., Frenk C.S., White S.D.M., et al., 2001, *MNRAS*, 321, 372
- Kaiser N., 1984, *ApJ*, 284, L9
- McCracken H.J., Ilbert O., Mellier Y., et al., 2008, *A&A*, 479, 321
- Mo H.J., White S.D.M., 1996, *MNRAS*, 282, 347
- Mo H.J., Jing Y.P., White S.D.M., 1997, *MNRAS*, 284, 189
- Navarro J., Frenk C., White S., 1997, *ApJ*, 490, 493
- Padilla N.D., Baugh C.M., Eke V.R., et al., 2004, *MNRAS*, 352, 211
- Peacock J.A., 1998, *Cosmological Physics*, Cambridge University Press
- Peebles P.J.E., 1980, *The large-scale structure of the universe*, Princeton University Press
- Peebles P.J.E., 1982, *ApJ*, 263, L1
- Peebles P.J.E., 1993, *Principles of Physical Cosmology*, Princeton University Press
- Pillepich A., Porciani C., Hahn O., 2009, arXiv:0811.4176
- Politzer H.D., Wise M. B., 1984, *ApJ*, 285, L1
- Prada F., Klypin A.A., Simonneau E., et al., 2006, *ApJ*, 645, 1001
- Press W.H., Schechter P., 1974, *ApJ*, 187, 425
- Reed D., Gardner J., Quinn T., et al., 2003, *MNRAS*, 346, 365
- Reed D.S., Bower R., Frenk C.S., Jenkins A., Theuns T., 2009, *MNRAS*, 394, 624
- Robertson B.E., Kravtsov A.V., Tinker J., Zentner A.R., 2009, arXiv:0812.3148
- Sheth R.K., Tormen G., 1999, *MNRAS*, 308, 119
- Sheth R.K., Mo H.J., Tormen G., 2001, *MNRAS*, 323, 1
- Tinker J., Kravtsov A.V., Klypin A., et al., 2008, *ApJ*, 688, 709
- Trujillo I., Conselice C.J., Bundy K., et al., 2007, *MNRAS*, 382, 109
- Valageas P., 2002a, *A&A*, 382, 412
- Valageas P., 2002b, *A&A*, 382, 450
- Valageas P., 2009a, *J. Stat. Phys.*, 134, 589
- Valageas P., 2009b, arXiv:0905.1910
- Valageas P., 2009c, arXiv:0903.0956
- Wang L., Steinhardt P.J., 1998, *ApJ*, 508, 483
- Warren M.S., Abazajian K., Holz D.E., Teodoro L., 2006, *ApJ*, 646, 881
- Zeldovich Y. B., 1970, *A&A*, 5, 84